This article has been accepted for publication in IEEE Transactions on Industry Applications. This is the author's version which has not been fully edited and content may change prior to final publication. Citation information: DOI 10.1109/TIA.2023.3289934

Finite Control Set Model Predictive Control for a Wheatstone Bridge Active Magnetic Bearing

Luca Tarisciotti, *Senior Member, IEEE*, Constanza Ahumada, *Member, IEEE,* Luca Papini, Catalina Gonzalez and Paolo Bolognesi

***Abstract*— Active Magnetic Bearing technology is becoming attractive for several reasons such as friction-free suspension and high-speed operation, high reliability, and vibration reduction. These desirable features come at the cost of the system's increased complexity, including position sensors, a power electronic converter, and a control system dedicated to the AMBs. This paper focuses on the control system design of an AMB featuring a Wheatstone bridge winding configuration and shaft position control. To achieve a high-bandwidth current control able to generate the desired forces, a Finite Control Set Model Predictive Control has been proposed in this paper. The AMB is modeled considering finite element simulation results to evaluate the relationship between inductance and rotor position and obtain the mechanical model parameters. A standard PI position control is also included in the system and tested under different scenarios. Finally, the control system is validated through simulation and Hardware-In-the-Loop experimental testing.**

***Index Terms*—Active Magnetic Bearing, Predictive Control, Power Conversion, DC/AC power conversion, Vibration control.**

I. Introduction

HIGH speed applications and direct drive systems are gaining importance in industry, and they are the subject of extensive research. The maximum achievable speed is mainly limited by the mechanical properties of materials, thermal issues, and bearings friction losses limitations. Considering the drive system of Fig. 1 (a), classical ball bearings, shown in Fig. 1 (b), are usually used at high speed with dedicated lubrication systems. These bearings are subjected to high wear and losses and do not allow any compensation of the shaft transversal vibrations. Several contactless technologies, such as gas, oil, or magnetic bearings, can be considered to improve these performances. These technologies are implemented with the aim of suspending the shaft at the center of its enclosure by applying a force resulting from air, oil, or magnetic force pressure as shown in Fig. 1 (c). However, even if it is possible to extend the bearings' life and reduce their losses, in applications where high vibrations are present, this solution may not be viable. On the other hand, Active Magnetic Bearings (AMBs), shown in Fig. 1 (d), generate the force necessary to lift and maintain the rotor centered using electromagnetic field pressure [1]. By controlling the AMB coils' current, it is possible to generate a variable force on the shaft which, not only keeps the rotor centered but can be potentially used to damp the vibrations generated by backlash and external perturbations [2].

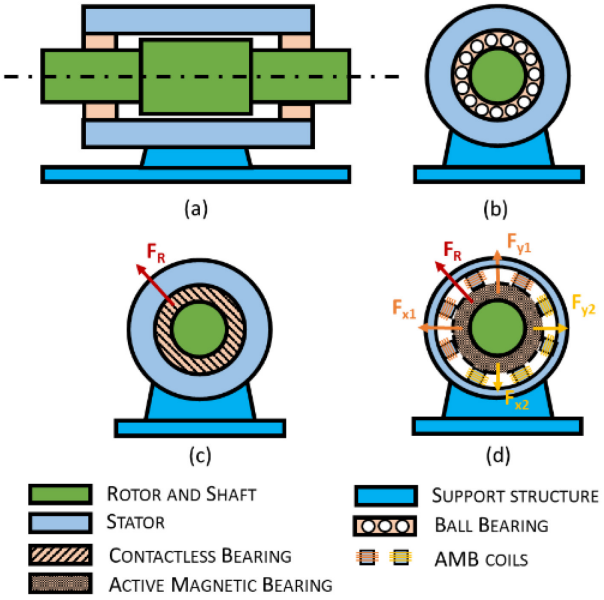

Fig. 1. Bearing technology for a drive unit: (a) Drive side view; (b) Ball bearing; (c) Contactless bearing (gas, oil, or permanent magnetic field); (d) Active Magnetic Bearing (AMB).

AMBs are particularly attractive for high-power as well as high-speed applications [3] and are becoming a valid alternative to standard roll-bearing for rotating machines [4], reducing losses and achieving a full active rotor-dynamic control of the system. In fact, AMBs are often considered as an alternative to standard roll-bearing [3], [4] and different magnetic bearing topologies have been proposed in the literature to reduce the vibrations on the shaft [5], to improve the force density and reduce losses [6]. The operative principle of AMBs is based on the flux density unbalance in the main airgap, which leads to a force acting on the rotor element generated by controlling the current flowing through the AMBs coils. The coil arrangement and control system adopted play a fundamental role in the performance of the system. A variety of coil numbers and

This work was supported by "Agencia Nacional Investigacion y Desarrollo" (ANID) through Projects:
FONDECYT Iniciación 11200121, FONDECYT Regular 1210208, FONDECYT Iniciación 11200866, FONDECYT Postdoctoral 3220126 and AC3E/BASAL FB0008.

Luca Tarisciotti is with the University Andres Bello, Santiago, Chile (e-mail: luca.tarisciotti@unab.cl).

Constanza Ahumada is with the University of Chile, Santiago, Chile (e-mail: coahumad@uchile.cl).

Luca Papini is with the University of Pisa, Pisa, Italy (e-mail: luca.papini@ing.unipi.it).

Catalina Gonzalez is with the University Andres Bello, Santiago, Chile (e-mail: catalina.gonzalez@unab.cl).

This article has been accepted for publication in IEEE Transactions on Industry Applications. This is the author's version which has not been fully edited and content may change prior to final publication. Citation information: DOI 10.1109/TIA.2023.3289934

arrangements can be found in literature exploiting the capabilities of three-phase systems to single-phase ones. In this work, the Wheatstone Bridge (WB) configuration for the AMB's power coil is considered [7], [8].

Clearly, an AMB system presents more components and circuitry with respect to a conventional bearing. Fig. 2 shows a schematic representation of the components needed, where the whole AMB system is split into three main areas: actuation, power electronics, and control.

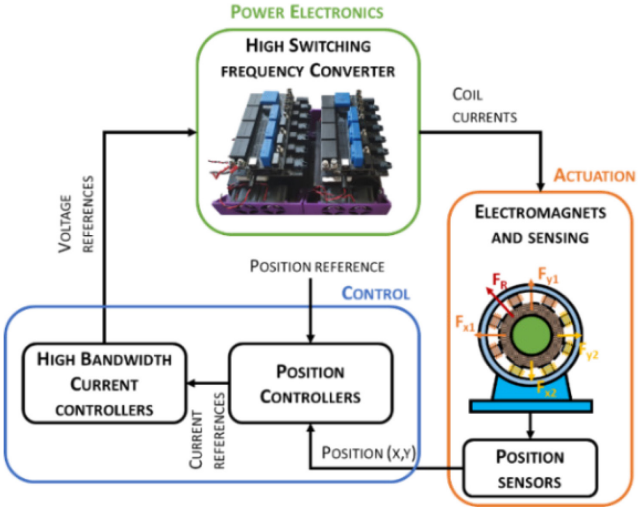

Fig. 2. AMB system block diagram

To control the coil currents, a power conversion system is required. The converter topology is related to the AMB coil arrangement, and several structures can be taken under consideration [8]–[13]. In this work such system is realized using a six-leg Voltage Source Converter (VSC) [9] which is particularly suitable for WB coil arrangements. The converter can control the biasing magnetizing flux density in the AMB through a DC current, identical in every coil, and control the rotor position over the *x* and *y* axes, by unbalancing the currents in the single AMB coils. However, since the six converter legs are connected to the same DC-Link and not isolated from the AMB coils, undesired circulating currents are present and must be suppressed by the current control. Due to the high bandwidth for the current controller, several techniques have been considered with the aim to minimize power dissipation [14], improve dynamic response [15] or increase robustness [12], [16], [17]. Among them, Model Predictive Control (MPC) can provide the desired performances, due to its inherently fast dynamic response and flexibility [18], [19]. MPC uses the system's mathematical model to predict its future behavior over a specific time horizon. Based on the prediction model, MPC solves a quadratic optimization problem by identifying the sequence of future actions which minimize a user-defined cost function. The best performing actuation is then applied, and all the calculations are repeated at every sample period. Since switching power converters are systems with a finite number of switching combinations, the MPC formulation can be reduced to evaluate state variables prediction and cost function minimization only for a discrete number of switching states [5]. This approach, named Finite Control Set Model Predictive Control (FCS-MPC), has been successfully applied for the current control in three-phase inverters [20]–[23], Multilevel [24], [25], DC/DC [26], [27] and Matrix converters [28], [29], as well as power control in an Active Front-End rectifier [20], and torque and flux control of an induction machine [30].

This paper proposes the application of FCS-MPC to the Current Control of a Wheatstone Bridge AMB driven by a six-leg VSC. The concept has already been proposed in [31] and this work provides additional Hardware-In-the-Loop (HIL) experiments that furtherly validate the control. Therefore, the contributions of this paper are:

- A comparison between the AMB analytical model and finite element model, which allows the implementation of the system by simulation.
- An FCS-MPC for the control of a WB AMB, which is validated by simulation and HIL considering real communication delays, as well as tested for systems with and without disturbances.
- A position control that is able to maintain stable operation under different scenarios such as external forces applied on the shaft, signal measurement noise, and communication delays.

It is important to highlight that, while FCS-MPC is a widely accepted control technique for power electronics, it has not been applied to this specific application where the current in all the eight AMB coils is controlled without being directly measured and just by controlling the currents in three single-phase inverters. This presents some challenges in the control implementation which are described in detail in the following sections. The rest of the paper is organized as follows. First, the AMB under study is modeled. In Section III the electrical system is described. In Section IV the proposed control is introduced. In Section V simulation results are presented, while in Section VI the experimental results are shown. Finally, in Section VII the conclusions are drawn.

II. AMB MODELING

There is a wide variety of possible structures for AMBs. Among all, the one considered in this work is inspired by [32], [33]. The structure features a 4-pole field generated in the stator-rotor clearance through currents flowing in the stator winding properly arranged. Aiming to achieve decoupled axis control, the active sides of each phase are arranged as depicted in Fig. 3.

The AMB is designed to achieve a peak force of 150 N. Inner rotor structure is selected and both the stator and rotor core are dimensioned to operate around the knee of the magnetization curve of the soft magnetic material. For the case study presented in this paper, the material features a saturation-knee flux density of 1.5 T and initial relative permeability of $4 \cdot 10^4$ H/m. The AMB is considered to operate without specific forced cooling methods and therefore the rated current density selected is limited to a current density J = 5 A/mm^2. The slot fill factor is assumed to be k_{fill} = 0.5 and the number of turns is computed to achieve the necessary Magneto-Motive-Force (MMF) in the air gap capable to develop the required force. The rotor is designed with a reduced magnetic load, to minimize the edgy currents in the

This article has been accepted for publication in IEEE Transactions on Industry Applications. This is the author's version which has not been fully edited and content may change prior to final publication. Citation information: DOI 10.1109/TIA.2023.3289934

laminations due to the high-frequency field variation. Each coil is considered wounded around a single stator tooth and is split into two parts. The total 8 coils are therefore located in the stator structure of which half are aligned with the x-axis and the other half with the y-axis. The coils belonging to each axis are arranged in a WB configuration. This allows unbalancing the air-gap magnetic field distribution super-imposing a differential current on a polarization one which flows in every coil. This can be done by means of controlling the 2 voltages imposed at the opposite nodes of the WB through power electronics devices as described in the following sections.

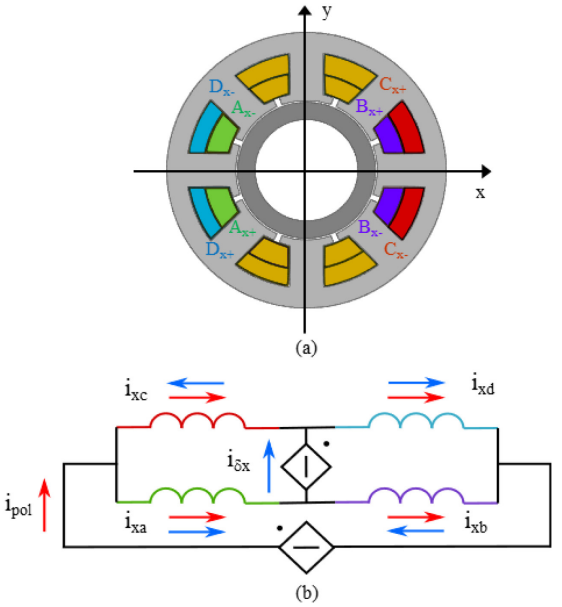

Fig. 3. (a) 2D model of the AMB (x-axis configuration) and (b) WB power coil arrangement for a single axis.

In [34] is presented a numerical model that can be used to characterize different AMB structures, highlighting the main features that characterize force generation in AMBs. It is shown that, approximating the model up to the first harmonic order, it is possible to focus on the inductance and their variation with respect to the rotor displacement amplitude, neglecting the effects that arise from the variation against the rotor displacement phase. Additionally, the inductance matrix can be modelled by a first order Fourier series achieving an accurate model. Finally, since the contribution of the inductance variation with respect to the phase angle of the displacement is negligible, therefore also the tangential force components provide a negligible contribution to the overall force generated by the AMB.

Therefore, aiming to assess the inductance with respect to the position of the barycenter of the rotor structure, the inductance matrix is computed considering the geometry and materials as listed in Table I. Combing all the above considerations, both analytical model and finite elements (FE) simulations are performed to characterize the dependency of the inductance of the AMB with respect to the rotor displacement. In particular, the characterization focuses on the description of the dependency of the inductances with respect to the x and y rotor displacement.

TABLE I. AMB PARAMETERS

DESCRIPTION	VALUE	UNIT
Rotor Outer Radius	22.25	[mm]
Air-gap thickness	0.4	[mm]
Axial length	21	[mm]
Number of turns	90	-

However, considering the decoupled axis design, the inductance values related to a single phase are computed only with respect to the displacement of the rotor in the direction of the magnetic axis of the coil considered. For rotor displacements up to 40% of the air gap, the ferromagnetic materials work in the linear region of their magnetic characteristic. With further increase of the displacement, saturation occurs on the side which features a reduced air gap due to the flux density concentration and the analytical model accuracy decreases. In this context, the elements of the inductance matrix can be expressed as in (1)

$$L_{kh}(\rho,\gamma) \cong L_{kh0}(\rho) + L_{kh1}(\rho)\, cos\,(\gamma) \qquad (1)$$

where γ is the displacement phase angle, while $L_{kh0}(\rho)$ and $L_{kh1}(\rho)$ are the amplitude of the mean and first harmonic. The analytical development of the Fourier Transform highlights the dependency of the coefficients with respect to the p.u. displacement ρ as reported in (2)

$$L_{kh0}(\rho) \propto \frac{1}{\sqrt{1-\rho^2}} \qquad L_{kh1}(\rho) \propto \frac{2}{\sqrt{1-\rho^2}} \left(\frac{1-\sqrt{1-\rho^2}}{\rho}\right) \qquad (2)$$

Fig. 4 depicts the comparison between FE and analytical inductance variation with respect to the amplitude of the displacement.

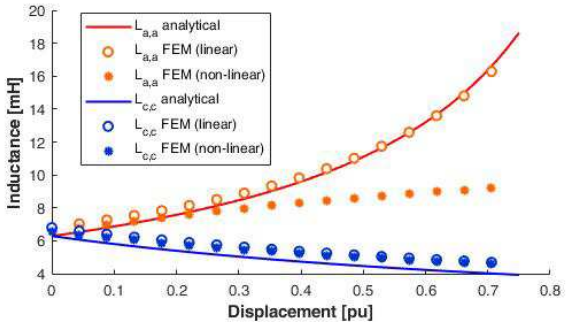

Fig. 4. FE and analytical model comparison of self-inductance of phase A and phase C with respect to the rotor displacement along the x-axis in p.u. of the airgap length.

For small displacements, the equations (1) and (2) can be substituted with the Taylor expansion around the origin of the functions leading to a constant average value (L_{kh0}) of the inductance with respect to ρ, while linear dependency is featured by the first harmonic element, i.e

$$L_{kh}(\rho) \cong L_{kh0}(1 + K_L\rho) \qquad (3)$$

In conclusion, due to the strong interaction of the coils with the magnetic circuit, the inductances of the coils are suitable to change in different operational conditions of the system. This is modeled and validated through FEA analysis, where also the saturation effect is accounted for. Considering the AMB design,

in the following analysis equation (3) is considered, with a nominal inductance value of L_{kh0} = 7mH and a rotor displacement variation ρ ± 0.5 p.u. and K_L = 1.

III. Electrical System Design and Modeling

Referring to Fig. 3, Fig. 5 shows the whole AMB electrical circuit. The AMB coils are electrically arranged as two WB connected in series. To operate properly, the system requires a polarizing current constantly flowing through the coils, which imposes the flux required to magnetize the system. When external forces are acting on the system, a variation of ±3 A in each AMB coil is imposed to unbalance the electromagnetic field thus resulting in electromagnetic forces developed from the AMB on the *x* and *y* axes, respectively. These forces allow maintaining the rotor in the equilibrium position under external mechanical disturbances. The system is controlled using three H-Bridges (HBs) fed by a common DC bus, as shown in Fig. 5.

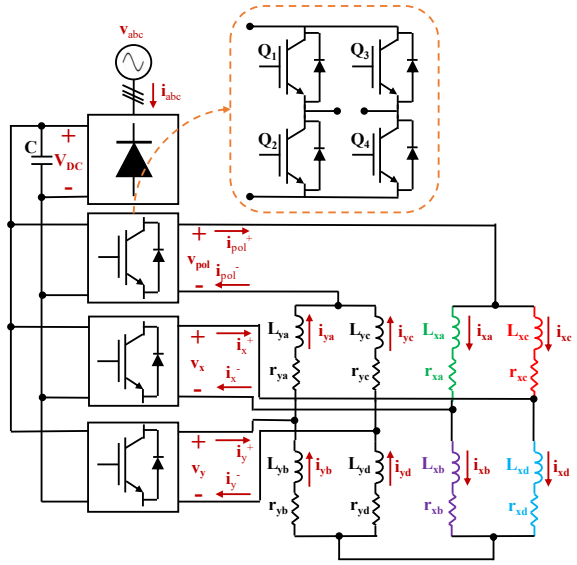

Fig. 5. WB power coil and inverter arrangement .

As shown in Fig. 5, the HB at the top is used to generate the polarizing current flowing through the WB legs while the second and third HBs generate a current unbalance in the AMB coils which allows to apply the electromagnetic force required on the x and y axes, respectively. Due to the AMB design, the system operates properly when the following constraints are satisfied:

$$\begin{cases} i_{xa} = i_{xd} \\ i_{xb} = i_{xc} \\ i_{ya} = i_{yd} \\ i_{yb} = i_{yc} \end{cases}, \quad \begin{cases} i_{pol}^{+} = i_{pol}^{-} = i_{pol} \\ i_{x}^{+} = i_{x}^{-} = i_{x} \\ i_{y}^{+} = i_{y}^{-} = i_{y} \end{cases} \tag{4}$$

These constraints are not imposed by the electrical circuit but rather by the current control system. By considering these constraints and applying Kirchoff's law to every node of the WB, the following expressions can be derived:

$$\begin{cases} i_{pol} = i_{xa} + i_{xc} = i_{xb} + i_{xd} \\ \quad\; = i_{ya} + i_{yc} = i_{yb} + i_{yd} \\ i_x = i_{xa} - i_{xb} = i_{xd} - i_{xc} \\ i_y = i_{ya} - i_{yb} = i_{yd} - i_{yc} \end{cases} \rightarrow \begin{cases} i_{pol} - i_x = i_{xb} + i_{xc} \\ i_{pol} + i_x = i_{xa} + i_{xd} \\ i_{pol} - i_y = i_{yb} + i_{yc} \\ i_{pol} + i_y = i_{ya} + i_{yd} \end{cases} \tag{5}$$

Moreover, the constraints given in (4) and, therefore, the ones given in (5), must be independently imposed on the three HBs by the converter control. Additionally, for control design purposes, controlling the current at the converter output represents a more practical solution, rather than directly measuring the WB coil's current. Finally, it is important to highlight that, while the coils' inductance varies with the rotor position, as described in the previous section, the inductance seen by each HBs does not vary, due to the arrangement of coils in the WB configuration. This allows avoiding the use of inductance estimation techniques in the current control system. Under the hypothesis of symmetric branches of the WB in a centered condition, the system can be described as follows:

$$\begin{cases} [S_{pol1} - S_{pol3}]V_{DC} = 2L\left[\frac{di_{pol}^{+}}{dt} + \frac{di_{pol}^{-}}{dt}\right] + 2r\left[i_{pol}^{+} + i_{pol}^{-}\right] \\ [S_{x1} - S_{x3}]V_{DC} = L\left[\frac{di_{x}^{+}}{dt} + \frac{di_{x}^{-}}{dt}\right] + r\left[i_{x}^{+} + i_{x}^{-}\right] \\ [S_{y1} - S_{y3}]V_{DC} = L\left[\frac{di_{y}^{+}}{dt} + \frac{di_{y}^{-}}{dt}\right] + r\left[i_{y}^{+} + i_{y}^{-}\right] \end{cases} \tag{6}$$

where L and r represent the nominal winding inductance and resistance of each AMB coil, respectively. Moreover, S_{ij} represents the state of the switch Q_j of the HB connected to the system $i \in \{pol, x, y\}$, respectively. S_{ij} has a value of 1 when the switch is on and 0 when the switch is off.

TABLE II. AMB Power Conversion System Nominal Parameters

NAME	DESCRIPTION	VALUE	UNIT
C	DC-Link capacitance	11	[mF]
L_{xa}, L_{xa}, L_{xc}, L_{xd}, L_{ya}, L_{yb}, L_{yc}, L_{yd}	Coils inductance	7	[mH]
r_{xa}, r_{xb}, r_{xc}, r_{xd}, r_{ya}, r_{yb}, r_{yc}, r_{yd}	Coils resistance	0.5	[Ω]
V_{DC}	DC-Link voltage	64	[V]
i_{pol}	Polarizing current	3	[A]
i_x, i_y	*x* and *y* HBs currents	± 3	[A]

For control design purposes, it is useful to split the model presented in (6) into six equations as follows:

$$\begin{cases} S_{pol1}V_{DC} = 2L\frac{di_{pol}^{+}}{dt} + 2ri_{pol}^{+} \\ -S_{pol3}V_{DC} = 2L\frac{di_{pol}^{-}}{dt} + 2ri_{pol}^{-} \\ S_{x1}V_{DC} = L\frac{di_{x}^{+}}{dt} + ri_{x}^{+} \\ -S_{x3}V_{DC} = L\frac{di_{x}^{-}}{dt} + ri_{x}^{-} \\ S_{y1}V_{DC} = L\frac{di_{y}^{+}}{dt} + ri_{y}^{+} \\ -S_{y3}V_{DC} = \frac{di_{y}^{-}}{dt} + Ri_{y}^{-} \end{cases} \tag{7}$$

where every controlled current depends only on the state of one HB leg. Table II shows the nominal parameters of the power conversion system under investigation.

IV. Control Design

The control system features two nested control loops. The outer loops are implemented as PID controllers which control the rotor position on the x and y axis, respectively. This control has been designed with a closed loop bandwidth of 113 Hz and outputs the current references for the x and y H-Bridge currents,

This article has been accepted for publication in IEEE Transactions on Industry Applications. This is the author's version which has not been fully edited and content may change prior to final publication. Citation information: DOI 10.1109/TIA.2023.3289934

which control the forces applied to the rotor. This means that the position control can reject disturbances with harmonic components up to 100 Hz. The FCS-MPC is used to implement the inner current control loop by regulating the currents on the x and y axis H-Bridges to the references provided by the PID controllers. Additionally, it controls the polarizing current necessary to magnetize the AMB and generate the required forces on the rotor. FCS-MPC controller is a nonlinear control with a bandwidth of 10kHz in this case, equal to half of the sampling frequency. It also features a specific implementation that allows controlling the AMB coil currents, and hence the forces applied to the rotor, by sensing only the H-Bridges AC currents. The FCS-MPC regulates the currents at the converter AC outputs by directly selecting the power electronic converter commutation state. Hence, this technique results in variable switching frequency, always lower than half of the sampling frequency and dependent on the source/load conditions.

In Fig. 6 the control block scheme for a single AMB is presented. The position control block considers a mechanical model and calculates the required HBs currents on the *x* and *y* axes, to achieve stable operative conditions. The control is implemented using a classical PID controller:

$$C_x(s) = C_y(s) = K_p + \frac{K_i}{s} + \frac{K_d s}{\frac{1}{K_f}s+1} \tag{8}$$

As can be noted from Fig. 6, the position control on the two axis is completely decoupled due to the specific coil arrangement in the AMB.

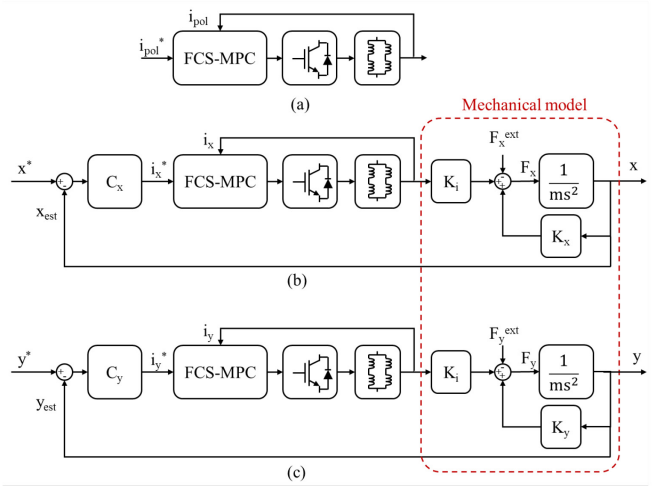

Fig. 6. Overall AMB system control scheme.

Regarding the current control, three separate controllers are used. One controller imposes the polarizing current through the WBs while the other two generate the necessary current unbalance in the AMB coils to respond to any mechanical disturbance with a fast and accurate transient.

Due to the high bandwidth required by the FCS-MPC current control, the whole control is implemented considering a control sampling frequency of 20 kHz. Using this configuration, it is possible to control the current in each of the WB coils. It should also be noted that, since FCS-MPC is used, the converter switching frequency is variable and always lower than half of the sampling frequency, making it feasible to use standard silicon power electronic devices. On the other hand, FCS-MPC requires the online evaluation of all the possible converter states, (64 for the system under study) and, thus, requires more computational resources than a classical PI current control implementation.

However, by defining the system electrical model as in (7), it is possible to simplify the control system and reduce the number of iterations required by FCS-MPC. Considering this model, FCS-MPC is independently implemented on the single HBs legs. The model in (7) is discretized using a forward Euler approximation of the derivative, at the sampling time T_s and using the discrete variable k as follows:

$$\begin{cases} i_{pol}^{+}(k+1) = i_{pol}^{+}(k) \quad + \frac{2L}{T_s}\left[S_{pol1}(k)V_{DC} - 2ri_{pol}^{+}(k)\right] \\ i_{pol}^{-}(k+1) = i_{pol}^{-}(k) - \frac{2L}{T_s}\left[S_{pol3}(k)V_{DC} + 2ri_{pol}^{-}(k)\right] \\ i_{x}^{+}(k+1) = i_{x}^{+}(k) \quad + \frac{L}{T_s}\left[S_{x1}(k)V_{DC} - ri_{x}^{+}(k)\right] \\ i_{x}^{-}(k+1) = i_{x}^{-}(k) - \frac{L}{T_s}\left[S_{x3}(k)V_{DC} + ri_{x}^{-}(k)\right] \\ i_{y}^{+}(k+1) = i_{y}^{+}(k) \quad + \frac{L}{T_s}\left[S_{y1}(k)V_{DC} - ri_{y}^{+}(k)\right] \\ i_{y}^{-}(k+1) = i_{y}^{-}(k) - \frac{L}{T_s}\left[S_{y3}(k)V_{DC} + ri_{y}^{-}(k)\right] \end{cases} \tag{9}$$

The discretized model is then used to predict the HBs currents at the discrete time instant *k+1* and is evaluated individually for every possible HB leg state. The state to be applied during the next sampling interval is then selected as the HB leg state that minimizes the following cost functions:

$$\begin{cases} G_{pol}^{+}(k+1) = \left|i_{pol}^{+}(k+1) - {i_{pol}}^{*}(k+2)\right| \\ G_{pol}^{-}(k+1) = \left|i_{pol}^{-}(k+1) - {i_{pol}}^{*}(k+2)\right| \\ G_{x}^{+}(k+1) = \left|i_{x}^{+}(k+1) - {i_{x}}^{*}(k+2)\right| \\ G_{x}^{-}(k+1) = \left|i_{x}^{-}(k+1) - {i_{x}}^{*}(k+2)\right| \\ G_{y}^{+}(k+1) = \left|i_{y}^{+}(k+1) - {i_{y}}^{*}(k+2)\right| \\ G_{y}^{-}(k+1) = \left|i_{y}^{-}(k+1) - {i_{y}}^{*}(k+2)\right| \end{cases} \tag{10}$$

The cost functions in (10) represent the tracking errors for each converter leg, where ${i_{pol}}^{*}$, ${i_x}^{*}$, and ${i_y}^{*}$ are the current references for the three HBs, respectively. It is worth mentioning that, since the currents on the single HB legs are controlled to minimize the error towards the same reference value, by using the cost functions in (10), the control inherently imposes the constraints in (4) which results in the desired converter behavior. This means that there is no current circulation through the three HBs that can therefore be considered independent converters, connected to separate DC-Links. Moreover, only two converter states for each HB leg need to be evaluated, resulting in a total of 12 converter states assessed at every sampling instant, reducing the computational burden, and easing the practical implementation.

V. Simulation Results

Simulations of the proposed system are carried out for two study cases using Plexim PLECS simulation software and the parameters given in Table I-IV. The position controller was designed to have $\xi = 0.8, t_s = 17.2\text{ms}, MOV = 1\%$, and $\omega = 276$ rad/s resulting in a closed-loop bandwidth of 113 Hz, while

This article has been accepted for publication in IEEE Transactions on Industry Applications. This is the author's version which has not been fully edited and content may change prior to final publication. Citation information: DOI 10.1109/TIA.2023.3289934

the FCS-MPC current controller has a sampling frequency of 20 kHz. The FCS-MPC sampling frequency as well as the PID position control bandwidth determine the maximum disturbance frequency that can be rejected by the control system and its response to pulsed disturbance. For example, AMBs are usually applied to high-speed motors, over 100.000 rpm, and high-frequency disturbances need to be suppressed. Another application case is when a lower speed is considered but external pulsating forces act on the rotor. Being the airgap in the order few points of mm, the control of the AMB system needs to act fast enough to avoid the rotor colliding with the stator. For these reasons, AMB systems usually require a performing control system which, together with the reduced number of iterations of the proposed FCS-MPC, makes its implementation feasible on a high-end DSP or SoC, although difficult on a commercial microcontroller.

TABLE III. CONTROL PARAMETERS

NAME	DESCRIPTION	VALUE	UNIT
K_p	Position control – Proportional gain	9870.5	[/]
K_i	Position control – Integral gain	486520	[/]
K_d	Position control – Derivative gain	47.9457	[/]
K_f	Position control – Derivative filter coefficient	50260	[/]
T_s	FCS-MPC current control Sampling frequency	20	[kHz]

In the first simulation, the control is analyzed for an ideal case in which no noise is present in the measured current signals and the rotor position is controlled to follow a circular pattern. Fig. 7 (a) and (b) show that no external forces are applied to the rotor while Fig. 7 (c) and (d), the rotor position in axis x and y are presented. Moreover, the position in both axes follows a sinusoidal shape as required by the controller. Thus, the controller can keep the rotor position stable at different values.

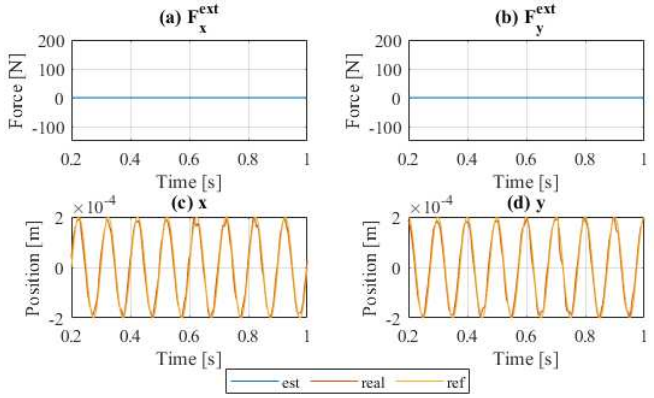

Fig. 7. AMB control following a position. (a) and (b) force applied to axes x and y. (c) and (d) position x and y.

In Fig. 8, the currents applied to the actuator are shown. The polarizing current i_{pol}, shown in Fig. 8 (a), is kept constant, while the current applied to the inductance i_x and i_y, and thus, also the current in the inductances i_a, i_b, i_c, i_d, slightly vary with the position changes. Moreover, the currents circulating in each inductance pair (i_a, i_c and i_b, i_d) have opposite sign, while current $i_b = i_a$ and current $i_c = i_d$ for each position.

In the second simulation, the sensitivity of the proposed control to noise and external perturbations is studied. With this aim, the rotor position is controlled to be kept constant to coordinates (0,0) with noise on current measurements included in the system. An external force with vibrations at 10Hz and 30Hz is applied to the rotor in both x and y directions to analyze the position control performance. Also, between 0.5s and 0.7s, a pulse is applied, representing a transient vibration force. Fig. 9 and Fig. 10 show the results obtained.

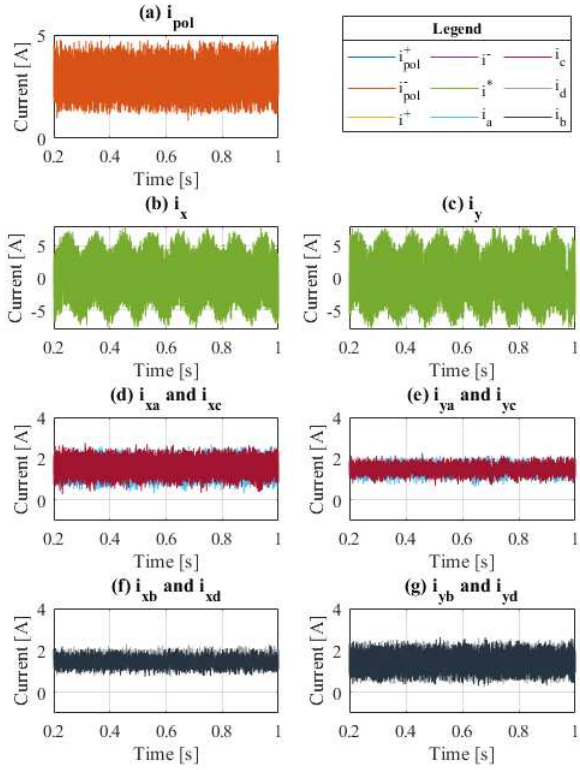

Fig. 8. AMB currents following a position. (a) Polarizing current. (b) and (c) current inyected to control the x and y position. (d) and (e) current in inductances L_a and L_c in axes x and y. (f) and (g) current in inductances L_b and L_d in axes x and y.

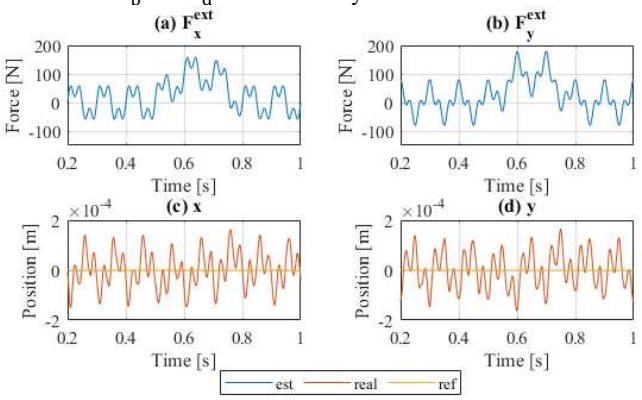

Fig. 9. AMB control with disturbance. (a) and (b) force applied to axes x and y. (c) and (d) position x and y.

In Fig. 9 (a) and (b), the forces applied in the x and y directions are shown. In Fig. 9 (c) and (d), the x and y position are presented, showing that the value oscillates around the reference value. This oscillation is produced by the perturbation applied to the system through the external forces acting on the rotor. Moreover, as shown in Fig. 9 (a) and (b), there is a force

impulse applied at 0.5s, which as seen in Fig. 9 (e) and (f) does not affect the position control. Analyzing the current in Fig. 10, it can be observed that when the pulse is applied, the current circulating in the inductances increases to maintain the rotor stable at (0,0) coordinates.

Fig. 11 shows the rotor trajectory in blue for different time instants in the two simulation cases. In Fig. 11 (a) the results obtained when the rotor follows a circular shape are presented, while in Fig. 11 (b), the results obtained when the rotor is controlled to remain at the center are shown. In both cases, the red line represents the safe operation area of 0.25mm, given an airgap of 0.5mm. As observed, in both cases, the rotor remains inside the safe operating area and follows the shape given.

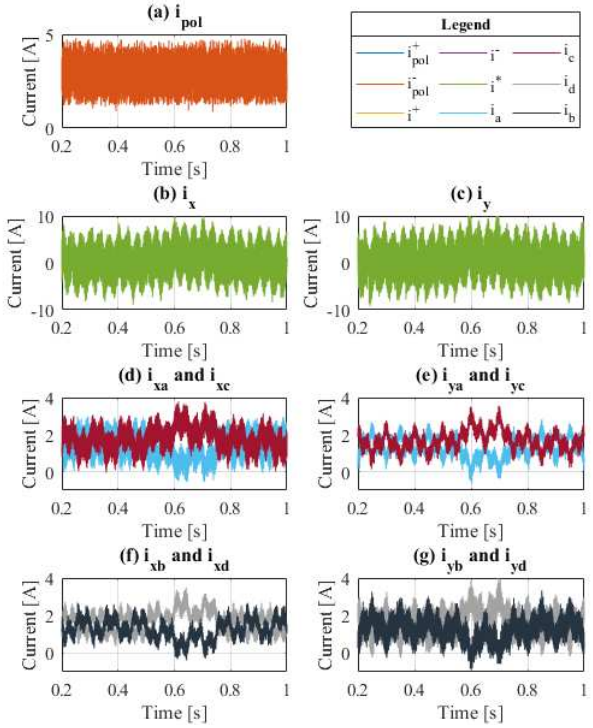

Fig. 10. AMB currents with disturbance. (a) Polarizing current. (b) and (c) current inyected to control the x and y position. (d) and (e) current in inductances L_a and L_c in axes x and y. (f) and (g) current in inductances L_b and L_d in axes x and y.

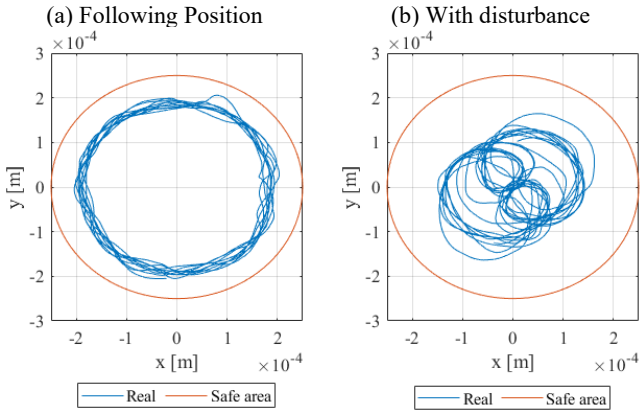

Fig. 11. x and y rotor position. (a) following a reference (b) with disturbance applied.

To further analyse the performance of the proposed system, the following scenarios are analysed. In Fig. 12 the effect of applying an impulsive force when the shaft is maintained at its central position is shown. In Fig. 13, the effect of a perturbation only in the vertical y-axis is presented. In Fig. 14, the AMB control with disturbance in the y-axis and following a position is presented. In Fig. 15 a white noise disturbance is applied while the shaft is controlled to follow a given position. Fig. 16 shows the y position relative to the x position for the 4 cases described.

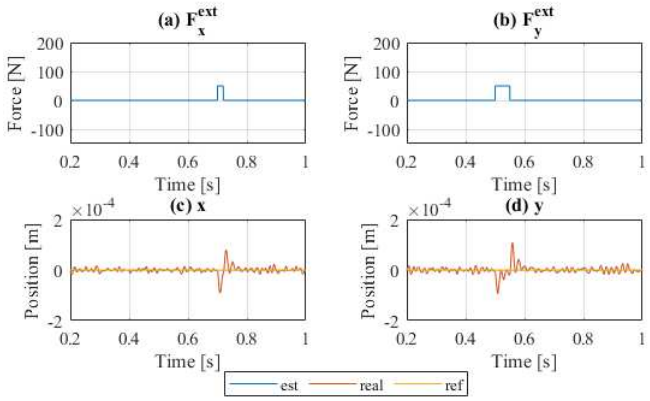

Fig. 12. AMB control with impulse disturbance. (a) and (b) force applied to axes x and y. (c) and (d) position x and y.

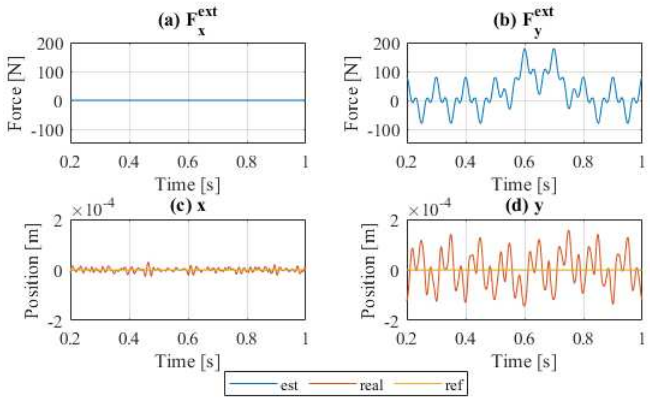

Fig. 13. AMB control with disturbance in y-axis. (a) and (b) force applied to axes x and y. (c) and (d) position x and y.

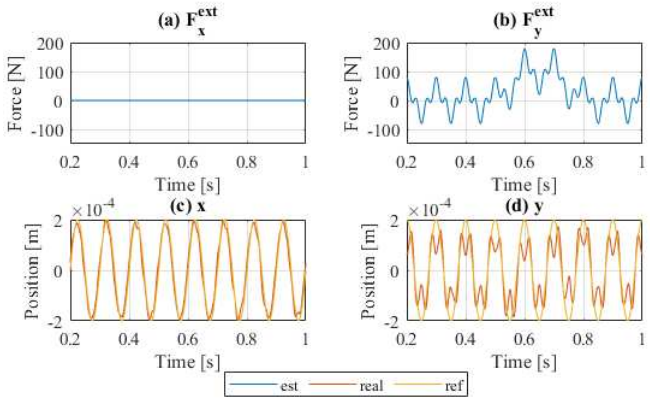

Fig. 14. AMB control with disturbance in the y-axis and following a position. (a) and (b) force applied to axes x and y. (c) and (d) position x and y.

This article has been accepted for publication in IEEE Transactions on Industry Applications. This is the author's version which has not been fully edited and content may change prior to final publication. Citation information: DOI 10.1109/TIA.2023.3289934

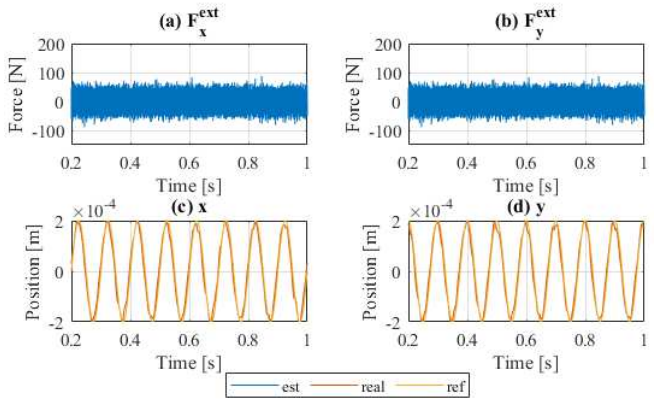

Fig. 15. AMB control with white noise disturbance and following a position. (a) and (b) force applied to axes x and y. (c) and (d) position x and y.

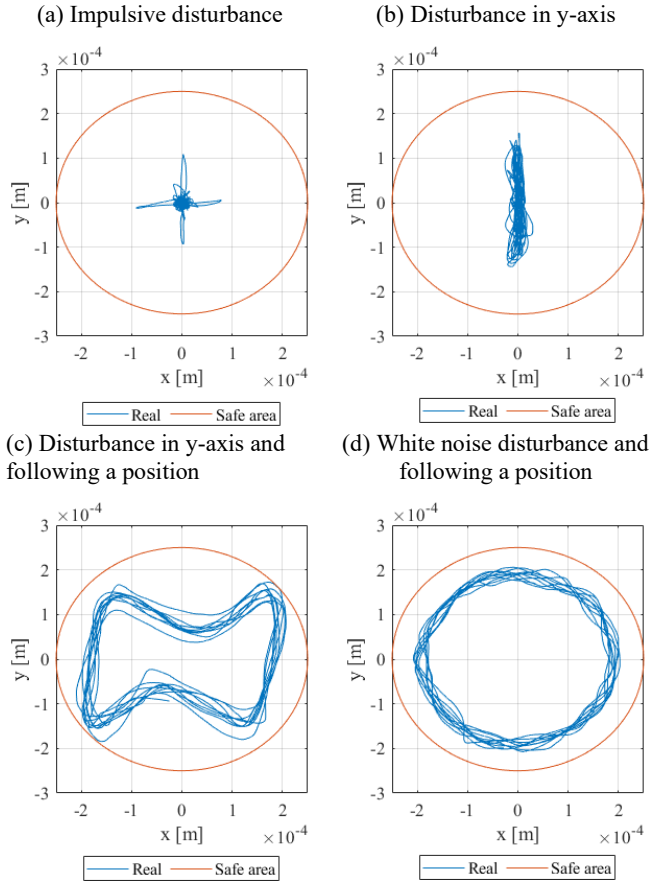

Fig. 16. AMB control with disturbance. (a) and (b) force applied to axes x and y. (c) and (d) position x and y.

It can be observed that in all the cases the AMB is able to keep the shaft inside the maximum allowed area, and maintain the shaft at the desired position regardless of the presence of different sources of external forces which act as perturbations. Therefore, it has been shown that the proposed control can follow and keep a given position in scenarios with different perturbation levels and operating with measurements subjected to noise, which is expected to be found in an experimental setup.

VI. Experimental Results

The experimental setup is shown in Fig. 17. It comprises a host PC that is used to program two independent Plexim PLECS RT-Box HIL simulators. In the first HIL simulator, only the control is included while the Plant model is loaded on the second RT-Box. The two simulators communicate with each other's using an SFP+ digital communication. No clock synchronization is performed between the two HIL simulators and, for this reason, can be considered operating independently. It is also worth mentioning that the RT-Box 1 use a Xilinx Zynq Z-7030 SoC, with the controller running on an ARM Cortex-A9 which has 1GHZ of clock frequency. This represents a powerful solution for advanced power electronics applications. Clearly, when compared to an industrial microcontroller, such as a Texas Instrument TMS320F28379D which has a clock frequency of 200MHz, the RT-Box is more powerful and performing. However, when considering custom solutions for advanced power electronics application, such as AMB applications, similar solutions based on the Xilinx Zynq architecture can be found in literature [35], [36].

The HIL model is implemented using the same parameters of Tables I to III and it includes the physical system and controllers' delay which affect the position controller behavior. In Fig. 18, the experimental implementation is shown in detail. Delays are included in the electrical system to decouple circuits with different time constants. This is a practice often applied in HIL implementation to ease the HIL software compiling and improve the execution speed. In this case, controlled voltage and current sources are used to emulate the voltage or current applied to each circuit, but clearly, a delay of one sampling step is necessary to avoid algebraic loops. Additionally, communication delays are considered on both RT-Box. The delays on the controller implementation consider one sampling interval delay at the controller input while the delays on the electromechanical models represent communication delays as well as the electrical circuit decoupling delays. Band-limited white noise is added to the measure at the control input, to represent a more realistic environment. Relevant signals, such as WB currents and rotor position are output using the HIL platform DAC and measured using oscilloscopes. It is important to highlight that the electromechanical system and the controller are executed at two different sampling frequencies. The controller is executed at 20kHz of sampling frequency which represents a realistic execution time on control hardware for AMB applications while the electromechanical system is executed at a sampling frequency of 400 kHz, representing a continuous time system.

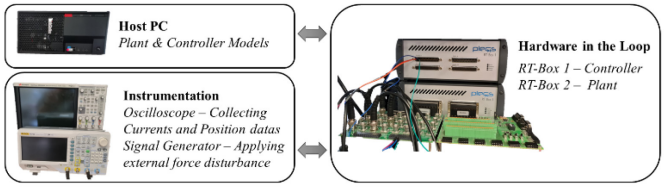

Fig. 17. Experimental setup.

Regarding the AMB and converter models, the switches are considered ideally commutated with dead-time implemented. Switches ON resistances are also considered. The AMB electrical circuit considers inductors with series resistance to represent the AMB coils. On the other hand, the mechanical system uses the electrical currents to calculate the forces applied to the rotor using the coefficient K_i. These forces are considered at the input of the mechanical system, together with external forces acting on the rotor and feedback forces calculated from the position using the coefficients K_x, K_y. All the coefficients are derived from FE simulations. The results obtained with this implementation are shown in Fig. 19 shows that when a sinusoidal force disturbance of amplitude +/- 150N at a frequency of 1Hz is applied. The control is able to generate the required current necessary to maintain the rotor in the centered position. When the frequency of the external force disturbance is increased to 10Hz in Fig. 20, the control is still able to operate but a residual oscillation of +/- 0.1mm is present, similar to the case when the external force disturbance of frequency 100Hz is applied in Fig. 21. However, it can be concluded that the control system is able to control the rotor position with minimal error. Additionally, the control has been tested to respond to external force step between -150N and 150N in Fig. 22 and 0N to 300N in Fig. 23. From the figures is possible to appreciate the minimal current control overshoot and the capability of the control of quickly reject the disturbance and reestablish the position on the x and y axis to their reference at coordinates (0,0).

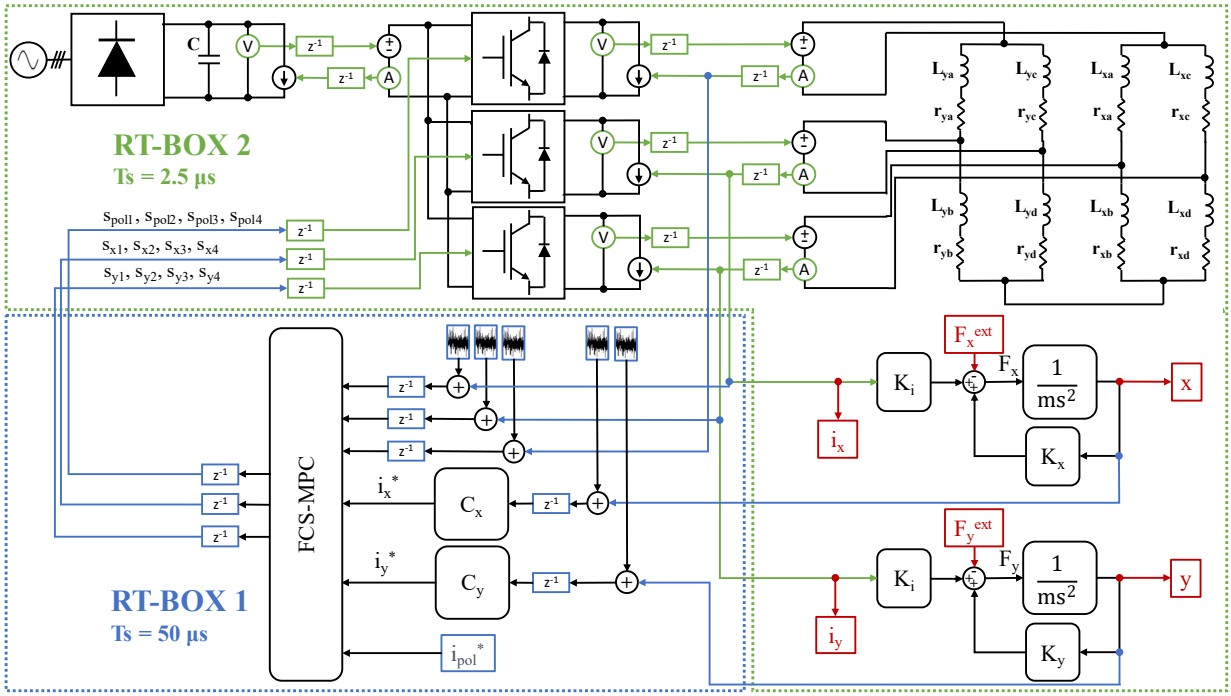

Fig. 18. HIL experimental implementation where delays at sampling times 2.5µs (in green) and 50 µs (in blue), band-limited white noise, and signal sent out through the platform DAC (in red) are highlighted.

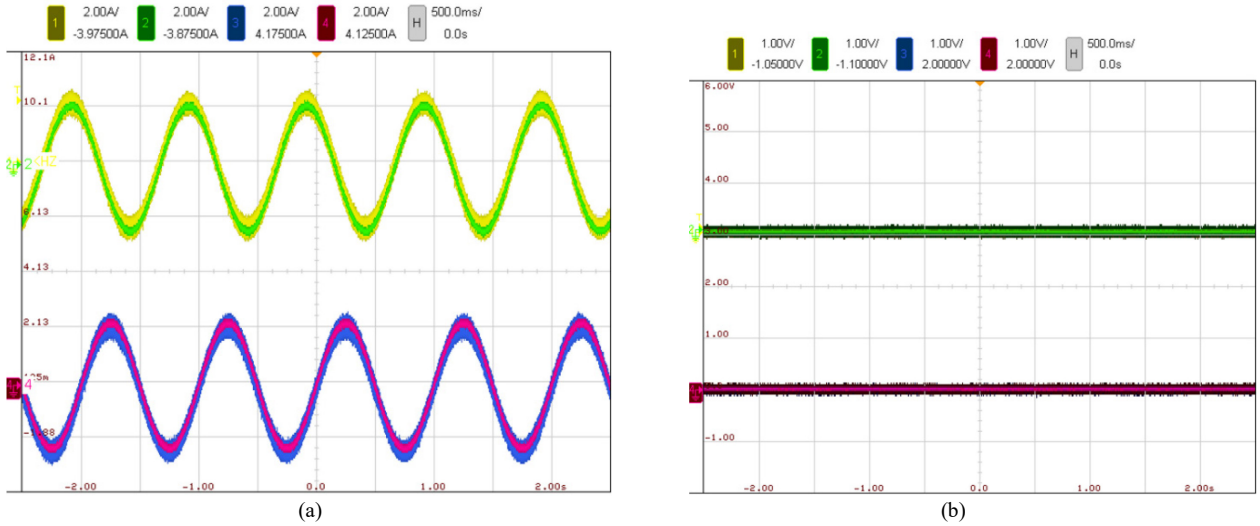

(a) (b)

Fig. 19. HIL results when a sinusoidal force disturbance of amplitude +/- 150N and frequency 1Hz is applied on both axes. (a) i_x (yellow), i_x^* (green), i_y (cyan) and i_y^* (blue) at 2.5A/div. (b) x (yellow), x^* (green), y (cyan) and y^* (blue) at 1mm/div.

This article has been accepted for publication in IEEE Transactions on Industry Applications. This is the author's version which has not been fully edited and content may change prior to final publication. Citation information: DOI 10.1109/TIA.2023.3289934

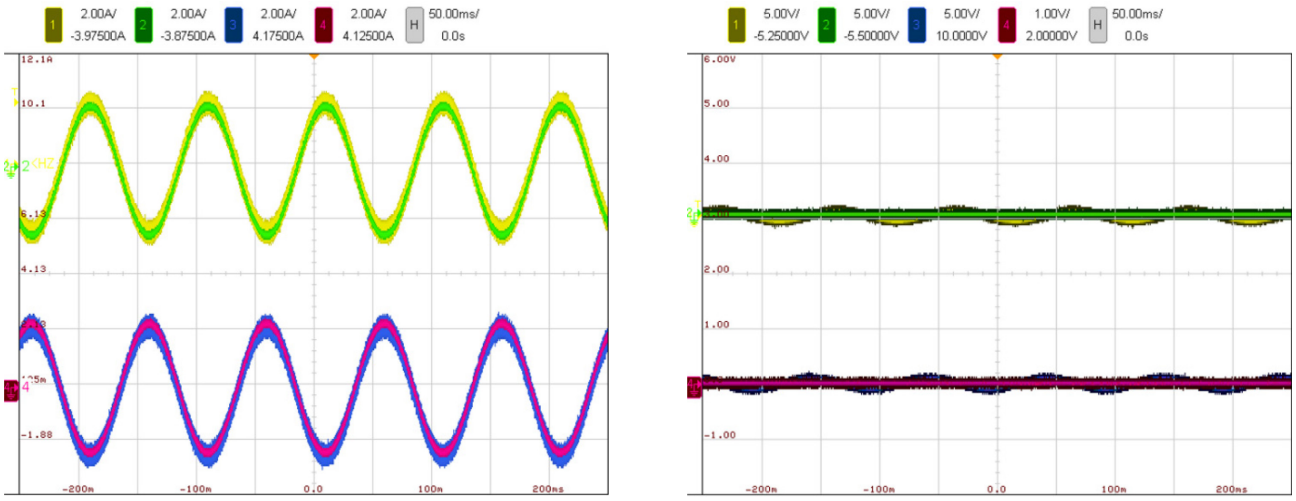

(a) (b)

Fig. 20. HIL results when a sinusoidal force disturbance of amplitude +/- 150N and frequency 10Hz is applied on both axes. (a) i_x (yellow), i_x^* (green), i_y (cyan) and i_y^* (blue) at 2.5A/div. (b) x (yellow), x^* (green), y (cyan) and y^* (blue) at 1mm/div.

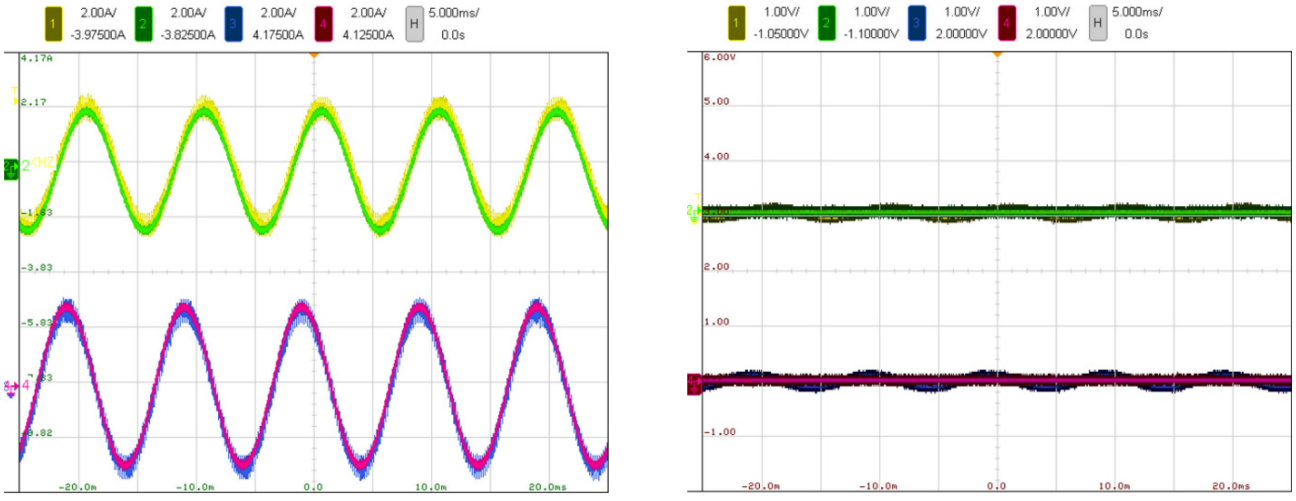

(a) (b)

Fig. 21. HIL results when a sinusoidal force disturbance of amplitude +/- 150N and frequency 100Hz is applied on both axes. (a) i_x (yellow), i_x^* (green), i_y (cyan) and i_y^* (blue) at 2.5A/div. (b) x (yellow), x^* (green), y (cyan) and y^* (blue) at 1mm/div.

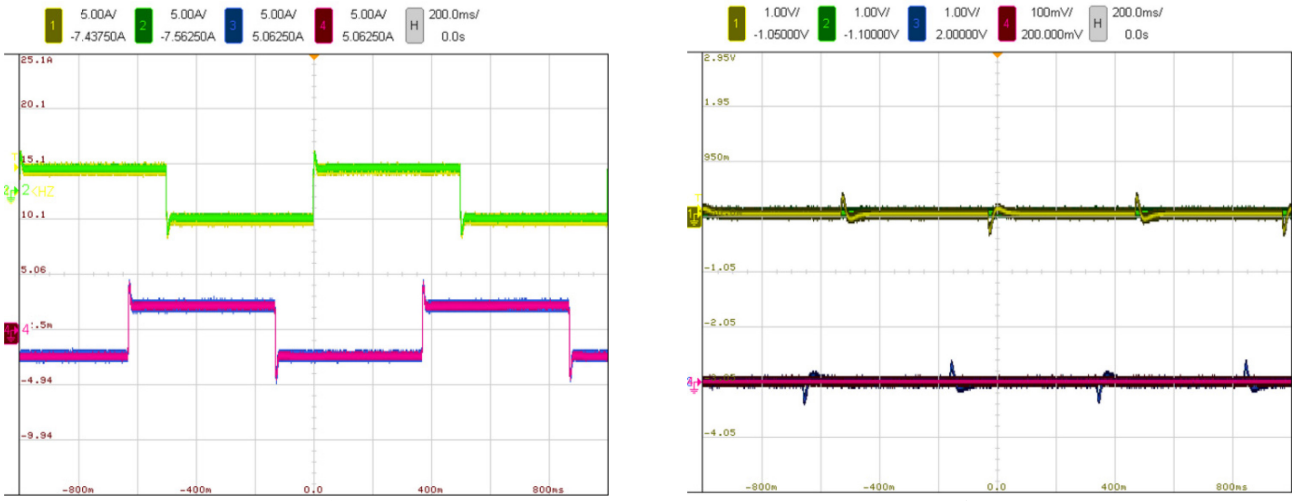

(a) (b)

Fig. 22. HIL results when a squared force disturbance of amplitude +/- 150 N at a frequency of 1Hz is applied on both axes. (a) i_x (yellow), i_x^* (green), i_y (cyan) and i_y^* (blue) at 2.5A/div. (b) x (yellow), x^* (green), y (cyan) and y^* (blue) at 1mm/div.

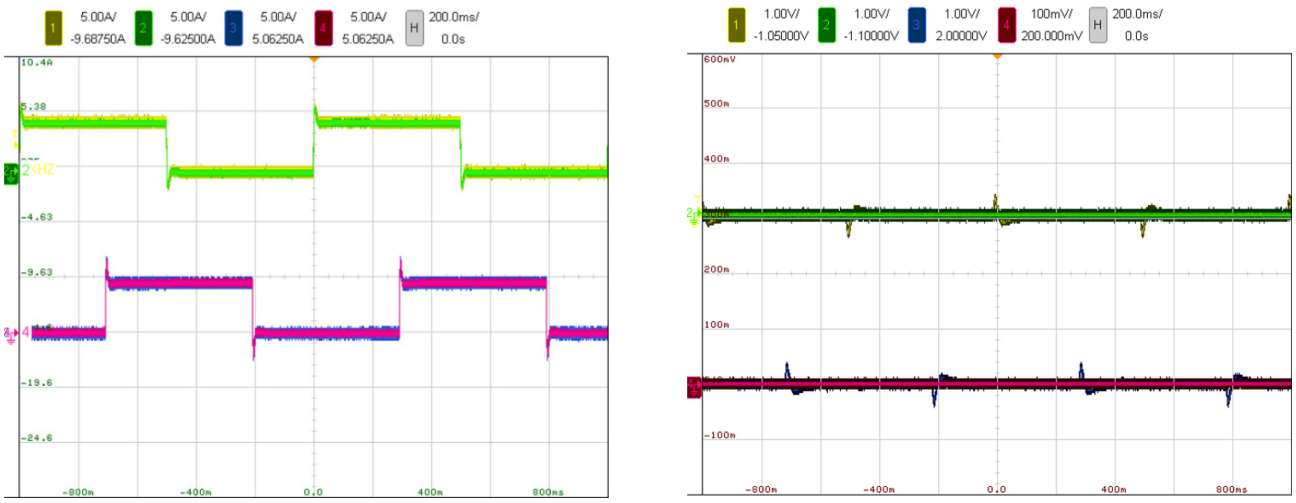

(a) (b)

Fig. 23. HIL results when a squared force disturbance of amplitude 300 N at a frequency of 1Hz is applied on both axes. (a) i_x (yellow), i_x^* (green), i_y (cyan) and i_y^* (blue) at 2.5A/div. (b) x (yellow), x^* (green), y (cyan) and y^* (blue) at 1mm/div.

VII. Conclusions

In this paper, FCS-MPC is applied to the power electronic conversion system for an AMB system, modeled as two WBs. The converter is composed of three HBs, which work independently and control the polarizing current flowing through the WBs and the current unbalance in the two WBs to apply the desired force on the rotor and maintain it stable in a centered position. In fact, the polarizing current magnetically loads the AMBs and by unbalancing the WBs leg currents it is possible to shift the rotor on the *x* or *y* machine axis, to respond to mechanical vibration and other disturbances. As these vibrations are usually in the order of hundreds of Hz, the current control requires a fast dynamic response and, for this reason, FCS-MPC is selected and the theoretical claims are supported by the simulation results, which show fast dynamic behavior for the current control. Simulation results also show good performance from the position control and its ability to work when band-limited white noise is present on the current measurement. Experimental tests on a HIL system composed of two Plexim RTBOX furtherly validate the theoretical claims by testing the proposed control in a realistic environment where communication, measurement, and actuation delays are considered.

References

[1] W. Zhang and H. Zhu, "Radial magnetic bearings: An overview," *Elsevier, Results in Physics*, vol. 7, pp. 3756–3766, 2017.

[2] G. Valente, L. Papini, A. Formentini, C. Gerada, and P. Zanchetta, "Radial Force Control of Multisector Permanent-Magnet Machines for Vibration Suppression," *IEEE Trans. Ind. Electron.*, vol. 65, no. 7, pp. 5395–5405, 2018, doi: 10.1109/TIE.2017.2780039.

[3] P. Imoberdorf, C. Zwyssig, S. D. Round, and J. W. Kolar, "Combined Radial-Axial Magnetic Bearing for a 1 kW, 500,000 rpm Permanent Magnet Machine," in *APEC 07 - Twenty-Second Annual IEEE Applied Power Electronics Conference and Exposition*, 2007, pp. 1434–1440.

[4] G. Schweitzer, "Active magnetic bearings—Chances and limitations," in *FTOMM nt. Conf. Rotor Dyn.*, 2002, pp. 1–12.

[5] P. Samanta and H. Hirani, "Magnetic Bearing Configurations: Theoretical and Experimental Studies," *IEEE Trans. Magn.*, vol. 44, no. 2, pp. 292–300, 2008, doi: 10.1109/TMAG.2007.912854.

[6] N. Motee, M. S. de Queiroz, Y. Fang, and D. M. Dawson, "Active magnetic bearing control with zero steady-state power loss," in *American Control Conference*, 2002, pp. 827–832.

[7] W. K. S. Khoo, K. Kalita, and S. D. Garvey, "Practical Implementation of the Bridge Configured Winding for Producing Controllable Transverse Forces in Electrical Machines," *IEEE Trans. Magn.*, vol. 47, no. 6, pp. 1712–1718, 2011, doi: 10.1109/TMAG.2011.2113377.

[8] J. Yang, D. Jiang, H. Sun, J. Ding, A. Li, and Z. Liu, "A Series-Winding Topology Converter With Capability of Fault-Tolerant Operation for Active Magnetic Bearing Drive," *IEEE Trans. Ind. Electron.*, vol. 69, no. 7, pp. 6678–6687, Aug. 2021, doi: 10.1109/tie.2021.3100983.

[9] K. Yang, Y. Hu, X. Guo, J. Zhou, and H. Wu, "Evaluation of Switching Power Amplifier Topology for Active Magnetic Bearings," *Actuators*, vol. 10, no. 6, p. 131.

[10] A. Kandil and Y. S. Hamed, "Tuned Positive Position Feedback Control of an Active Magnetic Bearings System with 16-Poles and Constant Stiffness," *IEEE Access*, vol. 9, pp. 73857–73872, 2021, doi: 10.1109/ACCESS.2021.3080457.

[11] J. Yang, D. Jiang, H. Sun, A. Li, and Z. Liu, "Series-Winding Topology Converter for Active Magnetic Bearing Drive," *IEEE Trans. Ind. Electron.*, vol. 68, no. 12, pp. 11772–11782, Dec. 2021, doi: 10.1109/TIE.2020.3040670.

[12] S. M. Amrr and A. Alturki, "Robust Control Design for an Active Magnetic Bearing System Using Advanced Adaptive SMC Technique," *IEEE Access*, vol. 9, pp. 155662–155672, 2021, doi: 10.1109/ACCESS.2021.3129140.

[13] T. Soni, J. K. Dutt, and A. S. Das, "Magnetic Bearings for Marine Rotor Systems-Effect of Standard Ship Maneuver," *IEEE Trans. Ind. Electron.*, vol. 68, no. 2, pp. 1055–1064, Feb. 2021, doi: 10.1109/TIE.2020.2967664.

[14] M. N. Sahinkaya and A. E. Hartavi, "Variable bias current in magnetic bearings for energy optimization," *IEEE Trans.*

Magn., vol. 43, no. 3, pp. 1052–1060, 2007, doi: 10.1109/TMAG.2006.888731.

[15] T. Schuhmann, W. Hofmann, and R. Werner, "Improving operational performance of active magnetic bearings using Kalman filter and state feedback control," *IEEE Trans. Ind. Electron.*, vol. 59, no. 2, pp. 821–829, 2012, doi: 10.1109/TIE.2011.2161056.

[16] G. R. Duan, Wu Zhan-Yuan, C. Bingham, and D. Howe, "Robust magnetic bearing control using stabilizing dynamical compensators," *IEEE Trans. Ind. Appl.*, vol. 36, no. 6, pp. 1654–1660, 2000, doi: 10.1109/28.887218.

[17] J. Li, G. Liu, P. Cui, S. Zheng, and Q. Chen, "Suppression of Harmonic Vibration in AMB-Rotor Systems Using Double-Input Adaptive Frequency Estimator," *IEEE Trans. Ind. Electron.*, vol. 69, no. 3, pp. 2986–2995, Mar. 2022, doi: 10.1109/TIE.2021.3065593.

[18] J. Rodriguez *et al.*, "Latest Advances of Model Predictive Control in Electrical Drives - Part I: Basic Concepts and Advanced Strategies," *IEEE Trans. Power Electron.*, vol. 37, no. 4, pp. 3927–3942, Apr. 2022, doi: 10.1109/TPEL.2021.3121532.

[19] J. Rodriguez *et al.*, "Latest Advances of Model Predictive Control in Electrical Drives - Part II: Applications and Benchmarking With Classical Control Methods," *IEEE Trans. Power Electron.*, vol. 37, no. 5, pp. 5047–5061, May 2022, doi: 10.1109/TPEL.2021.3121589.

[20] L. Tarisciotti, P. Zanchetta, A. Watson, J. C. Clare, M. Degano, and S. Bifaretti, "Modulated Model Predictive Control for a Three-Phase Active Rectifier," *IEEE Trans. Ind. Appl.*, vol. 51, no. 2, pp. 1610–1620, 2015.

[21] P. Cortés, G. Ortiz, J. I. Yuz, J. Rodríguez, S. Vazquez, and L. G. Franquelo, "Model predictive control of an inverter with output LC filter for UPS applications," *IEEE Trans. Ind. Electron.*, vol. 56, no. 6, pp. 1875–1883, 2009.

[22] L. Tarisciotti, P. Zanchetta, A. J. Watson, J. C. Clare, M. Degano, and S. Bifaretti, "Modulated Model Predictve Control (M2PC) for a 3-Phase Active Front-End," in *IEEE Energy Conversion Congress and Exposition (ECCE)*, 2013, pp. 1062–1069.

[23] L. Tarisciotti, G. lo Calzo, A. Gaeta, P. Zanchetta, F. Valencia, and D. Sáez, "A Distributed Model Predictive Control Strategy for Back-to-Back Converters," *IEEE Trans. Ind. Electron.*, vol. 63, no. 9, pp. 5867–5878, 2016, doi: 10.1109/TIE.2016.2527693.

[24] L. Tarisciotti, P. Zanchetta, A. Watson, J. Clare, and S. Bifaretti, "Modulated Model Predictive Control for a 7-Level Cascaded H-Bridge back-to-back Converter," *IEEE Trans. Ind. Electron.*, vol. 61, no. 10, pp. 5375–5383, 2014, doi: 10.1109/TIE.2014.2300056.

[25] L. Tarisciotti, P. Zanchetta, A. Watson, P. Wheeler, J. C. Clare, and S. Bifaretti, "Multiobjective Modulated Model Predictive Control for a Multilevel Solid-State Transformer," *IEEE Trans. Ind. Appl.*, vol. 51, no. 5, pp. 4051–4060, 2015, doi: 10.1109/TIA.2015.2429113.

[26] L. Chen *et al.*, "Predictive Control based DC Microgrid Stabilization with the Dual Active Bridge Converter," *IEEE Trans. Ind. Electron.*, vol. 0046, no. c, pp. 1–1, 2020, doi: 10.1109/tie.2020.2965460.

[27] L. Chen, S. Shao, Q. Xiao, L. Tarisciotti, P. W. Wheeler, and T. Dragičević, "Model Predictive Control for Dual-Active-Bridge Converters Supplying Pulsed Power Loads in Naval DC Micro-Grids," *IEEE Trans. Power Electron.*, vol. 35, no. 2, pp. 1957–1966, 2020, doi: 10.1109/TPEL.2019.2917450.

[28] L. Tarisciotti *et al.*, "Modulated Predictive Control for Indirect Matrix Converter," *IEEE Trans. Ind. Appl.*, vol. 53, no. 5, pp. 4644–4654, 2017.

[29] L. Tarisciotti *et al.*, "Model Predictive Control for Shunt Active Filters with Fixed Switching Frequency," *IEEE Trans. Ind. Appl.*, vol. 53, no. 1, 2017, doi: 10.1109/TIA.2016.2606364.

[30] S. S. Yeoh, T. Yang, L. Tarisciotti, C. I. Hill, S. Bozhko, and P. Zanchetta, "Permanent-Magnet Machine-Based Starter–Generator System With Modulated Model Predictive Control," *IEEE Trans. Transport. Electrific.*, vol. 3, no. 4, pp. 878–890, 2017.

[31] L. Tarisciotti, L. Papini, C. Ahumada, and P. Bolognesi, "Predictive Control For An Active Magnetic Bearing System With Sensorless Position Control," *IEEE Energy Conversion Congress and Exposition (ECCE)*, pp. 3267–3274, 2021, doi: 10.1109/ecce47101.2021.9595339.

[32] S. D. Garvey, G. Johnson, S. Pearson, K. Kalita, G. Moore, and A. Kirk, "Control of Rotors Suspended on Low-Cost Active Magnetic Bearings," *2019 IEEE International Electric Machines & Drives Conference (IEMDC)*, pp. 492–498, 2019, doi: 10.1109/IEMDC.2019.8785076.

[33] N. V. P. Kamisetti and G. Narayanan, "Electro-Magnetic Bearings with Power Electronic Control for High-Speed Rotating Machines: Review, Analysis and Design Example," *IEEE Trans. Ind. Appl.*, vol. 9994, no. c, pp. 1–1, 2021, doi: 10.1109/tia.2021.3093013.

[34] T. D'Aversa, L. Papini, and P. Bolognesi, "Fast Analytical-Numerical Modelling of Rotor Eccentricity for Radial Active Magnetic Bearing," *2021 IEEE Workshop on Electrical Machines Design, Control and Diagnosis (WEMDCD)*, pp. 70–75, 2021, doi: 10.1109/WEMDCD51469.2021.9425657.

[35] A. Jamal and G. Griepentrog, "Using System-on-Chip Boards for the Deployment of Controller for Verification and Prototyping," *2022 24th European Conference on Power Electronics and Applications (EPE'22 ECCE Europe)*, 2022.

[36] A. Galassini;, G. Lo Calzo;, A. Formentini;, C. Gerada;, P. Zanchetta;, and A. Costabeber, "uCube: Control platform for power electronics," *2017 IEEE Workshop on Electrical Machines Design, Control and Diagnosis (WEMDCD).*, 2017, doi: 10.1109/WEMDCD.2017.7947749.

This article has been accepted for publication in IEEE Transactions on Industry Applications. This is the author's version which has not been fully edited and content may change prior to final publication. Citation information: DOI 10.1109/TIA.2023.3289934

Luca Tarisciotti (S'12-M'15-SM'21) received the master's degree in electronic engineering from The University of Rome "Tor Vergata" in 2009 and his Ph.D. degree in Electrical and Electronic Engineering from the PEMC group, University of Nottingham in 2015. In the same year he became Research Fellow at the University of Nottingham, UK, until 2018 when he started working as Professor at the University of Chile, Santiago, Chile. From 2019 he is working as Associate Professor at the University Andres Bello, Santiago, Chile. His research interests include Matrix converters, DC/DC converters, Multilevel converters, advanced power electronics and Smart Grids control. During his academic career he published more than 90 papers in worldly recognized journal and conferences, contributing to several IEEE conferences organization as topic and session chair and serving as Associate Editor for IEEE Transaction on Industry Applications.

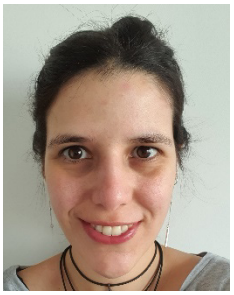

Constanza Ahumada (M' 18) received the B.Sc. and M.Sc. degrees in electrical engineering from the University of Chile, Santiago, Chile, in 2011 and 2013, respectively, and the Ph.D degree in electrical and electronic engineering from the University of Nottingham, Nottingham, U.K. in 2018. From the same year she has been an assistant professor with the Department of Electrical Engineering, University of Chile. From 2023 she is also an Associate Investigator in the research center AC3E, Chile. Her current research interests include electromechanical interaction and control strategies for the reduction of vibrations in aerospace, marine systems, and wind turbines.

Luca Papini received the bachelor's (Hons.) and master's (Hons.) degrees in Electrical Engineering from the University of Pisa, Italy, in 2009 and 2011, respectively, and the Ph.D. degree from the University of Nottingham, U.K., in 2018. He has been a Research Assistant with the University of Nottingham, since 2013. He was JSPS Fellow in 2018 and 2019, Senior Researcher at the University of Pisa from 2019 until 2022 and is currently Associate Professor at the University of Pisa. His research interests include modeling, analysis and testing of high-speed, high power density electric machines, machine control, multi-physics analysis and levitating systems.

C**atalina Gonzalez-Castaño** received the degree in electronic engineering from the Universidad Nacional de Colombia, Manizales, and the M.Eng. degree in Electrical Engineering from the Universidad Tecnológica de Pereira, Colombia in 2008 and 2013, respectively. And the Ph.D. (with honors) degree in electronic engineering in the field of power converters for electric vehicles from the Universitat Rovira i Virgili, Tarragona, Spain, in 2019. She is currently a researcher with Energy Transformation Center, Universidad Andres Bello, Santiago, Chile. Her main research interests are vehicular power systems, design and digital control of power converters, and green hydrogen production.

Paolo Bolognesi graduated in Electrical Engineering cum laude in 1995 at the University of Pisa and got his PhD with focus on power electronics in 1999 from the same University. In 2001 he joined the University of Pisa as an academic; he is presently a Senior Researcher and Appointed Professor in Electric Machines, Power Electronics and Electrical Drives. His research interests are mainly focused on the concept, modelling, design and control of electric machines, electromechanical devices and power converters featuring innovative topologies and advanced manufacturing solutions, to be used in different application fields spanning from industry automation to green transportation and renewables generation.